ELSEVIER

Journal of Structural Geology 27 (2005) 1765–1777

JOURNAL OF STRUCTURAL GEOLOGY

www.elsevier.com/locate/jsg

Application of three fault growth criteria to the Puente Hills thrust system, Los Angeles, California, USA

Erik L. Olson*, Michele L. Cooke

Department of Geosciences, University of Massachusetts Amherst, 611 North Plesant Street, Amherst, MA 01003-9297, USA

Received 25 August 2004; received in revised form 20 January 2005; accepted 9 February 2005
Available online 31 August 2005

Abstract

Three-dimensional mechanical models are used to evaluate the performance of different fault growth criteria in predicting successive growth of three échelon thrust faults similar to the segments of the Puente Hills thrust system of the Los Angeles basin, California. Four sequential Boundary Element Method models explore the growth of successive échelon faults within the system by simulating snapshots of deformation at different stages of development. These models use three criteria, (1) energy release rate, (2) strain energy density, and (3) Navier–Coulomb stress, to characterize the lateral growth of the fault system. We simulate the growth of an échelon thrust fault system to evaluate the suitability of each of these criteria for assessing fault growth. Each of these three factors predicts a portion of the incipient fault geometry (i.e. location or orientation); however, each provides different information. In each model, energy release rate along the westernmost (leading) tip of the Puente Hills thrust drops with growth of the next neighboring fault; this result supports the overall lateral development of successive échelon segments. Within each model, regions of high strain energy density and Navier–Coulomb stress envelope at least a portion of the next fault to develop, although the strain energy density has stronger correlation than Navier–Coulomb stress to the location of incipient faulting. In each model, one of the two predicted planes of maximum Navier–Coulomb stress ahead of the leading fault tip matches the strike but not the dip of the incipient fault plane recreating part of the fault orientation. The incipient fault dip is best predicted by the orientation of the strain energy density envelopes around the leading fault tip. Furthermore, the energy release rate and pattern of strain energy density can be used to characterize potential soft linkage (overlap) or hard linkage (connection) of échelon faults within the system.

Keywords: Échelon fault propagation; Energy release rate; Strain energy density; Naviér–Coulomb stress; Puente Hills thrust

1. Introduction

How do fault systems grow? Although the mechanics of opening mode fractures is well-understood and the theoretical underpinnings of opening-mode fracture propagation have been used to simulate this type of fracturing in a wide range of environments (e.g. Pollard and Aydin, 1988), the mechanics of fault growth remains enigmatic. Within the brittle crust, at least three different criteria for characterizing macroscopic fault propagation have been proposed: (1) energy release rate (2) strain energy density, and (3) Navier–Coulomb stress. Energy release rate, G, calculated along fault tips measures the propagation potential of the fault, with high values of energy release rate indicating greater propagation potential (e.g. Lawn, 1993; Kattenhorn and Pollard, 1999; Willemse and Pollard, 2000). Strain energy density measures the elastic strain energy stored in the host rock around the faults (e.g. Jaeger and Cook, 1976). Higher strain energy density values may arise in areas experiencing inelastic deformation such as microcracking, which facilitate fault growth (Du and Aydin, 1993; Cooke and Kameda, 2002). Navier–Coulomb stress also measures the failure potential of intact rock and can be used to predict the location and orientation of the possible failure planes (e.g. Jaeger and Cook, 1976; Crider and Pollard, 1998; Maerten and Pollard, 2002; Ferrill and Morris, 2003). Although each of these criteria is used to predict fault growth, no studies have compared the results of all three criteria within the same fault system.

To compare the three fault growth criteria we simulate the growth of an échelon thrust fault system whose

* Corresponding author. Present address: BP-Amoco, Houston, TX, USA.
E-mail address: erikolson2@gmail.com (E.L. Olson).

0191-8141/$ - see front matter © 2005 Elsevier Ltd. All rights reserved.
doi:10.1016/j.jsg.2005.02.005

three-dimensional configuration is remarkably well-constrained, the Puente Hills thrust system of the Los Angeles basin (Fig. 1). Shallow seismic reflection data have provided extraordinary detail of the Puente Hills thrust fault geometry above 5 km depth (Shaw et al., 2002) and geometry at deeper levels is constrained by relatively coarse seismic data (Shaw and Suppe, 1996; Shaw et al., 2002), seismicity (Shaw and Shearer, 1999) and mechanical validation studies (Griffith and Cooke, 2004). Furthermore, the seismic evidence of syn-deformational strata suggests that the three blind thrust fault segments that comprise the thrust system may have evolved sequentially from east to west (Shaw, personal communication, 2003).

By numerically modeling the lateral evolution of an échelon thrust system based on the Puente Hills thrust system, we evaluate the predictive capabilities of the three failure criteria. At several stages of fault system growth we examine the incipient fault geometry (location and orientation) predicted by energy release rate, strain energy density and Navier–Coulomb stress. The criteria best suited for predicting the échelon fault geometry studied here could be implemented to simulate observed (analog) and interpreted (geologic) fault growth in other fault systems.

2. Fault growth studies

Many recent geologic and analog-experiment studies investigating the nature of fault system growth demonstrate that large faults develop from the propagation and linkage of smaller fault segments (e.g. Gupta et al., 1998; Marchal et al., 1998; Dawers and Underhill, 2000; Kattenhorn and Pollard, 2001; Young et al., 2001; Maerten and Pollard, 2002; Meyer et al., 2002; Childs et al., 2003; Pivnik et al., 2003). The seismic expression of syn-deformational strata reveals the linkage of fault segments in the North Sea (Gupta et al., 1998; Dawers and Underhill, 2000), the Timor basin (Childs et al., 2003) and the Suez Rift (Pivnik et al., 2003). Slip distributions on faults in southern England also suggest fault growth by segment linkage (Kattenhorn and Pollard, 2001). Extensional fault evolution within analog devices show the initiation of many faults at inferred points of weakness followed by fault segment propagation and linkage to produce larger faults (e.g. Marchal et al., 1998; Mansfield and Cartwright, 2001). Along with abundant linkage, geologic evidence from the Timor basin shows lateral propagation of faults that varies temporally during fault system evolution (Meyer et al., 2002; Childs et al., 2003). Much of this evidence suggests that each of the échelon fault segments within systems such as the Puente Hills Thrust do not develop in isolation.

Despite the abundance of geologic and analog evidence for fault growth by propagation and linkage, few studies have numerically investigated fault system growth (e.g. Spyropoulos et al., 2002). By prescribing the mechanics of fault propagation, numerical simulation of observed (analog) and interpreted (geologic) fault growth could test our understanding of fault growth. In part, the dearth of fault growth models is caused by the complex nature of fault growth and subsequent gaps in our mechanical understanding of fault growth. For example, the development of mature fault surfaces is the product of abundant microcracking and linking of cracks (e.g. Scholz, 2002). The empirical (e.g. Navier–Coloumb) and theoretical (e.g.

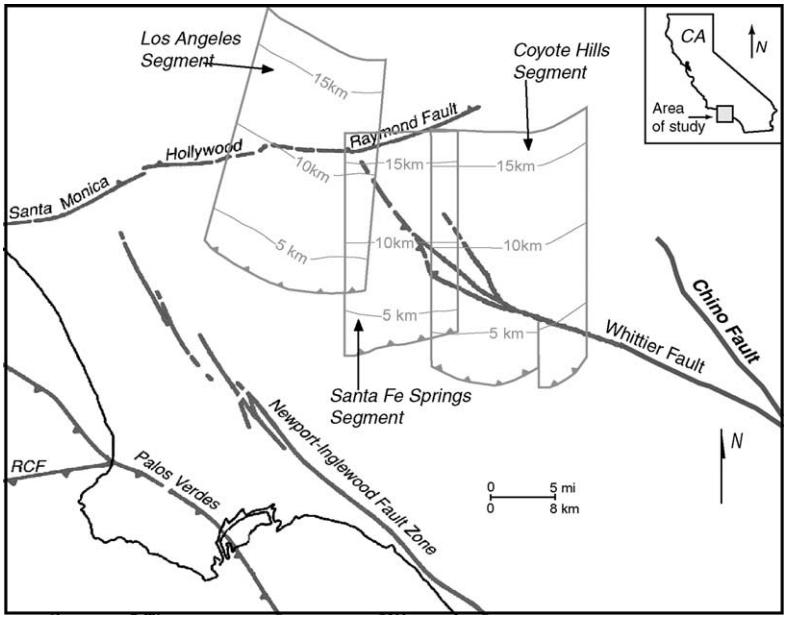

Fig. 1. Active faults of the Los Angeles Basin. The surface traces of the major faults including the Whittier and Chino faults are outlined. The blind faults of the Puente Hills thrust system: Los Angeles, Santa Fe Springs, and Coyote Hills segments, are shown with structure contours. None of the three segments of the Puente Hills thrust system reach the surface.

energy release rate and strain energy density) criteria for fault propagation used in this study overlook the micro-processes in order to assess the overall growth of faults. In this study we seek to assess the suitability of three empirical and theoretical fault growth criteria in the successive development of échelon thrust fault systems by simulating lateral growth of the Puente Hills thrust system.

3. Geologic setting of the Puente Hills thrust system

The Los Angeles basin began forming in the late Miocene (e.g. Wright, 1991; Ingersoll and Rumelhart, 1999). Basin subsidence at that time was accommodated by large extensional faults including the Whittier–Elsinore fault system and the Santa Monica fault system (Fig. 1; e.g. Wright, 1991). In the mid-Pliocene the relative plate motion between the North American plate and the Pacific plate changed to produce overall north–south compression of the basin (e.g. Wright, 1991). This compression led to the development of a series of blind thrust faults in the young sediments of the Los Angeles basin, including the Puente Hills thrust system (e.g. Wright, 1991).

The Coyote Hills, Santa Fe Springs, and Los Angeles faults are the three blind fault segments, with no surface trace, that comprise the Puente Hills thrust system (Fig. 1). The potential seismic hazard of these faults to the metropolitan Los Angeles was demonstrated in 1987 when the Santa Fe Springs ruptured in the M 6.0 Whittier Narrows earthquake (Shaw and Shearer, 1999). Geologic evidence suggests the Puente Hills thrust system as a whole is capable of generating earthquakes greater than M 7.0, and has caused four such events over the past 11,000 years (Dolan et al., 2003).

The relative age of the Puente Hills thrust fault segments is not yet fully resolved. Seismic reflection evidence of folded strata overlying the faults suggests that the Los Angeles segment is the youngest of the faults and the Coyote Hills fault segment appears to have the longest record of activity (Shaw, personal communication, 2003). This geologic evidence is consistent with an overall westward development of fault segments within the Puente Hills Thrust system. On the other hand, the deformation attributed to the westernmost Los Angeles segment of the Puente Hills thrust could alternatively be interpreted as reactivation of the older Las Cienegas Fault described by Schneider et al. (1996) and Wright (1991) (Meigs and Cooke, 2004). In the absence of definitive evidence for one or the other interpretations, our model simulates westward development of successive segments of the échelon thrust fault system.

Faults have been observed to develop through the interaction, linkage and synchronous growth of smaller faults within extensional basins (e.g. Dawers and Underhill, 2000; Young et al., 2001; Childs et al., 2003; Pivnik et al., 2003; Walsh et al., 2003) and analog experiments (e.g. Marchal et al., 1998; Mansfield and Cartwright, 2001). We have no reason to suspect that the fault segments of the Puente Hills thrust did not also grow in this manner and further analysis of the seismic reflection data may provide more detailed constraints on the growth and interaction of each fault segment. However, for the purpose of this study, we simulate the overall westward development of the system in four snapshots, ignoring the details of individual fault segment growth.

4. Numerical modeling

This study employs numerical modeling through the Boundary Element Method code Poly3D (Thomas, 1993) to explore factors affecting fault growth. Poly3D uses continuum mechanics to analyze a homogeneous linear elastic system, which provides an adequate approximation for behavior of faulted rock at shallow crustal levels over short time periods (e.g. 5000 years). Unlike the Finite Element Method, which requires discretization of the entire body, the Boundary Element Method only requires discretization of fault surfaces. This is advantageous for modeling multiple faults because the Boundary Element Method requires less effort for discretization, and errors due to discretization and approximation arise only along fault surfaces (Crouch and Starfield, 1990). Boundary Element Method codes, such as Poly3D, have been used for modeling three-dimensional fault interaction (e.g. Crider and Pollard, 1998; Willemse and Pollard, 2000; Kattenhorn and Pollard, 2001; Maerten and Pollard, 2002; Griffith and Cooke, 2004).

In order to explore the evolution of the fault system we use four models that each represent a 5000-year snapshot within the 6 million year development of the Puente Hills thrust. This time span exceeds the known earthquake recurrence time on faults of the region (e.g. Dolan et al., 1995) so that the models incorporate at least one complete earthquake cycle on the modeled faults without exceeding the 1% strain limitations of infinitesimal linear elastic strain analysis.

For each model, several parameters remain fixed. Every model simulates remote contraction at a rate of 72×10^{-9}/year at 006.5° and zero east–west contraction (Feigl et al., 1993) over 5000 years. Of the present-day contraction directions calculated from geodetic data within the Los Angeles basin, the north–south contraction determined by Feigl et al. (1993) and Argus et al. (1999) accompanied by zero east–west contraction best accounts for geologic observations of right slip on the Whittier and San Gabriel faults (Griffith and Cooke, in press). Although the contraction direction of the Los Angeles basin is likely to have fluctuated over the past several million years during the development of the Puente Hills thrust, the details of these fluctuations are not available. Consequently, we apply the modern contraction direction for all of our models.

Variation in contraction rate only alters the magnitude of the energy release rate and strain energy density, and does not alter the patterns. The Young's modulus is 30,000 MPa and Poisson's ratio is 0.25 to represent an average of the material properties in this portion of the Los Angeles basin (Griffith and Cooke, 2004). The geometry of the fault surfaces was obtained from the Community Fault Model of the Southern California Earthquake Center (http://structure.harvard.edu/cfma). All of the faults are modeled as frictionless surfaces that do not move apart.

Model 1 precedes development of the Puente Hills thrust and each subsequent model adds an additional Puente Hills thrust fault segment in their complete present day geometry. A greater number of model increments, simulating the piecewise growth of the faults, could more accurately simulate evolution of the system, which is likely to involve some degree of synchronous growth and linkage (e.g. Marchal et al., 1998; Mansfield and Cartwright, 2001). However such constraints on fault growth are not available for the Puente Hills thrust at this time. Consequently, this study focuses on the lateral propagation of the fault system with the addition of whole fault segments from east to west.

The Whittier and Chino faults are the only two faults in model 1. The entire length of the Whittier fault is not included within the model because this study concerns the fault's western tip. The eastern tip of the Whittier fault is placed far enough away to not affect the western tip (Fig. 2). The Chino fault is a strike-slip fault, similar to the Whittier fault, and dips to the southwest, intersecting the Whittier fault (Fig. 2). The Chino fault is included in this study because the fault may play a role in the distribution of slip on the Whittier fault, subsequently influencing stresses in the Puente Hills thrust region.

Model 2 includes the Coyote Hills fault, along with the Whittier and Chino faults. The Coyote Hills fault is a blind thrust fault, which dips approximately 30° to the north and intersects the western edge of the Whittier fault. The portion of the Whittier fault in the footwall of the Coyote Hills thrust appears to remain active to the base of the seismogenic crust (Griffith and Cooke, 2004).

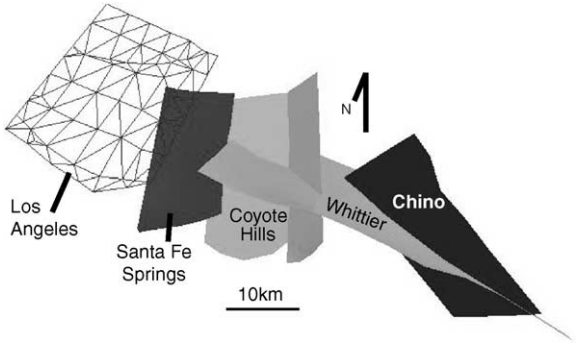

Fig. 2. Map view of the modeled Puente Hills thrust system, along with the Whittier and Chino faults. The Los Angeles segment is shown as a wire frame to illustrate the fault mesh used in the Boundary Element Method model.

Model 3 in the evolutionary series includes the Whittier, Chino, Coyote Hills, and Santa Fe Springs faults. The Santa Fe Springs thrust lies immediately west, with some échelon overlap, of the Coyote Hills fault, and lies approximately along the same trend as the Whittier and Coyote Hills faults. The Santa Fe Springs fault has a similar orientation to the Coyote Hills fault, but is not as laterally extensive.

All three of the faults of the Puente Hills Thrust system are included in model 4, along with the Whittier and Chino faults. The Los Angeles fault, located northwest of the Santa Fe Springs fault, is slightly échelon and right-stepping relative to the Santa Fe Springs fault. The western tip of the Los Angeles fault either terminates against or intersects the Hollywood and Raymond faults (Fig. 1; Shaw et al., 2002). These faults are not included in the models of this study because they are not part of the Puente Hills thrust.

5. Energy release rate

The mode II and mode III stress intensity factors (KII and KIII, respectively) describe the relative magnitudes of the shearing and tearing mode stress concentrations acting on the tips of each fault, respectively. KII is based on the slip perpendicular to the crack tip, and KIII is based on slip parallel to the crack tip (Thomas and Pollard, 1993; Willemse and Pollard, 2000):

$$K_{\mathrm{II}} = 0.806 \frac{\mu\sqrt{2\pi}}{4(1-\nu)} \frac{\Delta u_{\mathrm{III}}}{\sqrt{r}} \tag{1}$$

$$K_{\mathrm{III}} = 0.806 \frac{\mu\sqrt{2\pi}}{4} \frac{\Delta u_{\mathrm{III}}}{\sqrt{r}} \tag{2}$$

where μ is shear modulus, Δu_{II} and Δu_{III} are slip in mode II and mode III, respectively, on the element at the fault tip, and r is the distance from the element center to the edge of the element. The stress intensity factors along a fault tip line can be combined to calculate the energy release rate, G (e.g. Lawn, 1993):

$$G = \frac{(1-\nu)}{2\mu}\left[K_{\mathrm{I}}^2 + K_{\mathrm{II}}^2 + \frac{1}{(1-\nu)}K_{\mathrm{III}}^2\right] \tag{3}$$

where ν is Poisson's ratio, K_{I} is the opening mode stress intensity factor and μ is the shear modulus. High values of G suggest greater likelihood for fault propagation so that where the energy release rate exceeds the empirically determined energy required for the creation of new fault surface, G_c, the fault propagates (e.g. Lawn, 1993; Kattenhorn and Pollard, 1999; Willemse and Pollard, 2000; Scholz, 2002). The G_c for various rock types, measured by triaxial experiments is on the order of 10^1–10^4 J/m^2 (Wong, 1982; Li, 1987); however, pure mode III cracks fail at lower G_c, on the order of 10^1–10^2 J/m^2 (Cox and Scholz, 1988). The lateral edges of thrust faults considered in this study are expected to experience primarily mode III

deformation ($K_{III} > K_{II}$) and may fail at the lower range of these G_c measurements.

Faults have propagation potential along their entire tip-lines and generally propagate along the portions that have the greatest propensity for propagation. The location of greatest propagation potential depends on many factors including fault geometry, interaction with neighboring faults (Willemse and Pollard, 2000), as well as tectonic and lithostatic stress field (Kattenhorn and Pollard, 1999). Along reverse faults, such as the Puente Hills thrust, the upper and lower tips will have propagation potential, as will the lateral tips. However, this study is concerned with the lateral growth of the Puente Hills thrust system, so the energy release rate at the top and bottom tips of the fault is ignored. Similarly, energy release rate of the eastern tips of the Whittier and Chino faults and the western tip of the Los Angeles fault are not considered because they are not relevant to the Puente Hills thrust system evolution and, furthermore, these tips are influenced by other faults not considered in the model. By measuring the lateral propagation potential of each Puente Hills thrust fault segment we do not mean to imply that each fault propagates to become the next adjacent segment. The seismic data indicate that these échelon segments are distinct to a depth of 5 km. Rather, we use energy release rate to measure the overall potential for lateral growth of the Puente Hills thrust system. Potential linkage of the fault segments at depth is discussed later in the paper.

5.1. Energy release rate results

The western tip of the Chino and Whittier faults experience no change in propagation potential with the development of the Puente Hills thrust system (Fig. 3A and B). This result is consistent with geologic evidence that neither the Whittier nor the Chino fault has propagated during the growth of the Puente Hills thrust over the past 4–6 million years (Wright, 1991). Along the west tip of the Chino fault G decreases from 33 J/m^2 at the Earth's surface to 4 J/m^2 at the base of the fault. Throughout all four models, the values of energy release rate along the west tip of the Whittier fault have the highest value of 20 J/m^2 at the top of the fault, and the lowest value near 4 J/m^2 at the base of the fault.

For all of the faults, the drop in energy release rate with depth along the lower half of the faults is a consequence of the manner in which fault tips are modeled at the base of the seismogenic crust (Fig. 3). Slip is required to approach zero at fault tips where material ahead of the tip sustains no slip (e.g. also evidenced in the slip-rate patterns of Figs. 4 and 5). Although this condition is accurate for the upper tips of the blind thrust faults, the lower tips are likely to transition into a zone of diffuse strain. Consequently the actual slip rate along the lower half of the faults will likely be greater than modeled here.

The Coyote hills fault is included in models 2–4, and the most significant changes in energy release rate occur on the western tip with the addition of the adjacent Santa Fe Springs fault (Fig. 3C). Propagation potential is unchanged along the shallow portion of the fault, but by 8 km depth there is a 2 J/m^2 difference between model 2 and models 3 and 4. Below 7 km depth, the western tip of the Coyote Hills fault has consistently lower energy release rate with the addition of subsequent faults. The maximum difference in energy release rate between models 2 and 3 is 8 J/m^2 at 10 km depth. The energy release rate along the eastern tip of the Coyote Hills fault increases slightly with the addition of the Santa Fe Springs and Los Angeles faults (Fig. 3D).

The Santa Fe Springs fault is included in models 3 and 4, and G along both eastern and western tips changes between the models. The energy release rate along the eastern tip of the Santa Fe Springs fault increases with the addition of the Los Angeles fault (Fig. 3F). The maximum increase in energy release rate is 6 J/m^2 near 9.5 km depth. The energy release rate tapers out up and down along the lateral tip of the fault so that propagation potential is small at the top and bottom of the fault. Additionally the value of energy release rate at 9.5 km depth on the eastern tip of Santa Fe Springs fault is the second highest in all of the models, 27 J/m^2 in model 3 and 33 J/m^2 in model 4. On the western tip of the Santa Fe Springs fault, the energy release rate decreases with the addition of the Los Angeles fault (Fig. 3E). This decrease occurs primarily below a depth of 7 km, with a maximum decrease of 5 J/m^2.

The Los Angeles fault is only examined in model 4, so only one set of energy release rate values is graphed for the eastern tip (Fig. 3G). The eastern tip of the Los Angeles fault has a low overall energy release rate.

5.2. Energy release rate analysis

The range of energy release rate accumulated in 5000 years of modeled deformation on all lateral fault tips (5–35 J/m^2; Fig. 3) overlaps with the critical values for failure on pure mode III cracks (10–100 J/m^2, Cox and Scholz, 1988). This suggests that some portions of the lateral tips might propagate upon 5000 years of loading whereas other portions require greater time to accumulate stresses leading to failure. Rather than focusing on the values of energy release rate, we focus instead on the patterns and changes in energy release rate between models. We expected the energy release rate to be highest on the western tips of each fault, where a large amount of slip may foreshadow the growth of a new fault. In contrast to our expectations, the four fault tips with the greatest energy release rate values (Chino, Whittier and eastern edges of Coyote Hills and Santa Fe Springs) are not those adjacent to incipient Puente Hills thrust faults (Fig. 3).

Two points of greatest energy release rate occur at the surface of the western tips of the Chino and Whittier faults. The propagation potential along these tips remains high throughout all the models, suggesting that both the Whittier

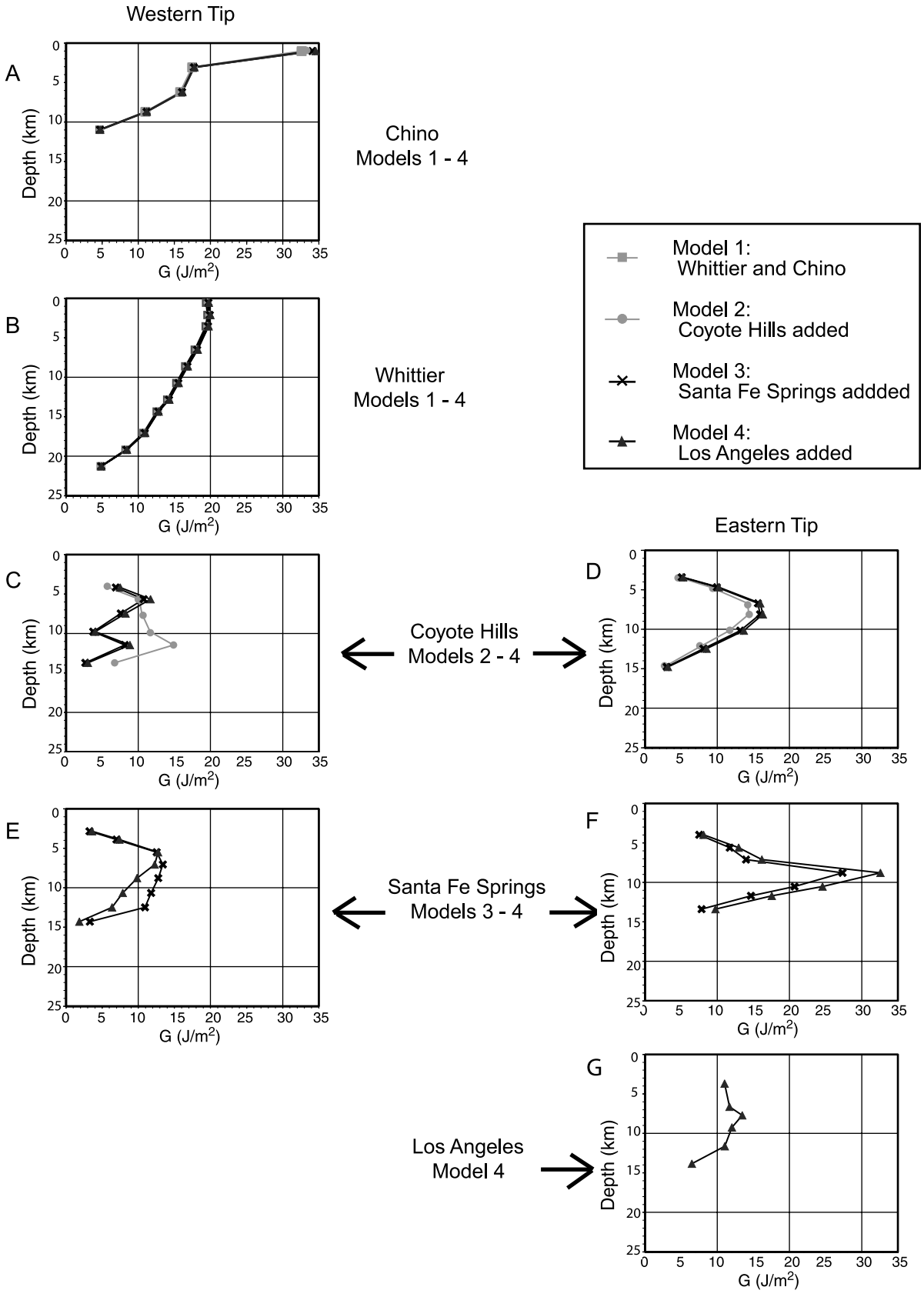

Fig. 3. Energy release rate for each of the lateral fault tips considered in this study. The Chino and Whittier faults (A and B) are included in all four models. The Coyote Hills fault (C and D) is included in models 2–4. Note the decrease in energy release rate along the western (leading) tips of the Coyote Hills fault with the addition of the Santa Fe Springs Fault (C) and also the Santa Fe Springs fault with the addition of the Los Angeles fault (E). The eastern (overlapped) tips Santa Fe Springs and Coyote Hills faults have high energy release rate (D and F) suggesting that these faults may propagate farther eastward than modeled, perhaps linking with adjacent faults.

and Chino faults may propagate further than modeled. However, the models of this study leave out some known faults from the region northwest of the Chino and Whittier faults (e.g. Alhambra Wash and San Jose faults; Fig. 1). With inclusion of additional faults in this region, the energy release rate along the western edges of the Chino and Whittier faults may decrease.

The high energy release rate along the eastern edges of the Coyote Hills and Santa Fe Springs faults may be better understood by examining the distribution of slip on these faults (Figs. 4 and 5). The eastern half of the Coyote Hills fault shows a pronounced component of strike-slip and relatively large net slip magnitudes. Isolated thrust faults undergoing dip-parallel contraction are not expected to have a significant component of strike-slip. Therefore, the location and distribution of strike-slip on the Coyote Hills fault reflects interaction with the adjacent Whittier and/or Chino strike-slip faults. Strike-slip may be transferred from the Whittier to the Coyote Hills fault producing high slip along the eastern edge of the Coyote Hills fault, which promotes eastward propagation of the fault. Eastward propagation of the Coyote Hills could lead to a hard linkage between this and the Whittier and/or Chino faults. This type of hard linkage of overlapping faults via propagation within

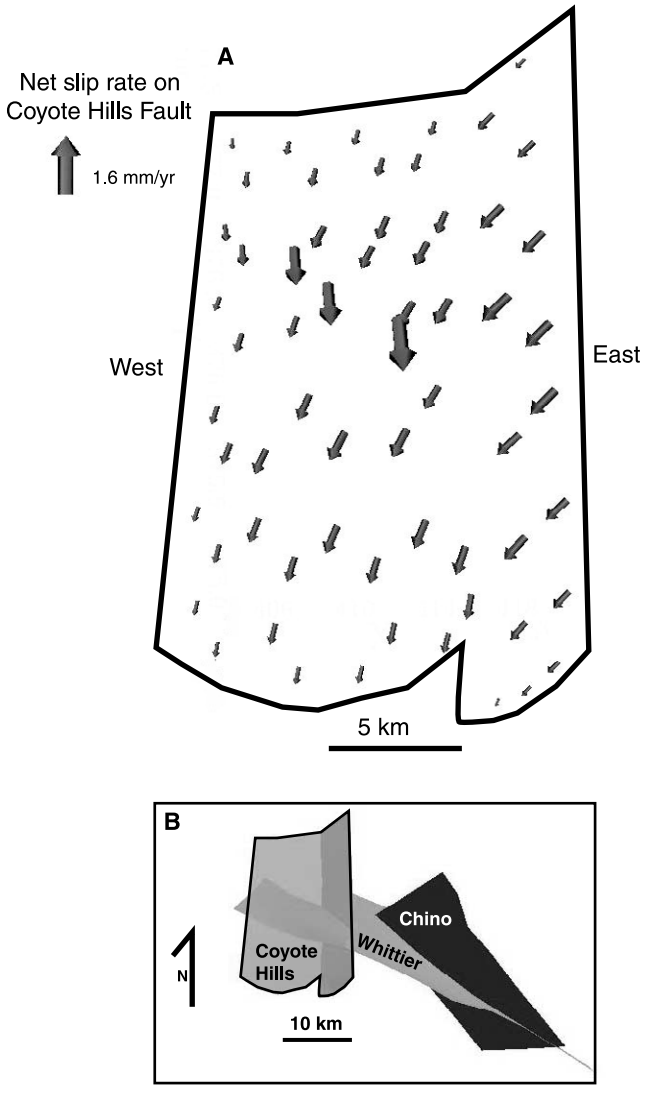

Fig. 4. Map view of slip vectors (A) on the Coyote Hills fault in model two (B). The arrows are scaled and shaded to show slip velocity. The trend of the vectors indicates primary dip-slip with significant strike-slip along the eastern portion of the fault. Note the asymmetric pattern of slip with fastest net slip and strike-slip halfway down the eastern tip of the fault due to interaction with the Chino and/or Whittier faults. Transfer of slip from the adjacent faults to the east produces greater energy release rate on the eastern edge of the Coyote Hills fault than the western (leading) edge.

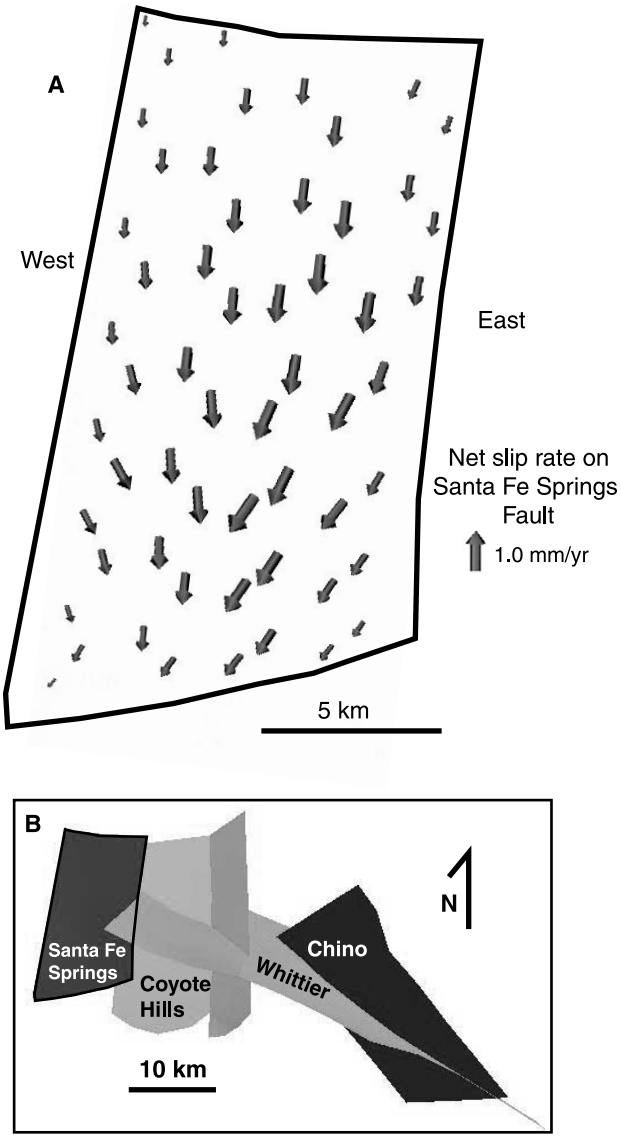

Fig. 5. Map view of slip vectors (A) on the Santa Fe Springs fault in model 3 (B). The arrows are scaled and shaded to show slip velocity. The trend of the vectors indicates primary dip-slip with significant strike-slip. Note the asymmetric pattern of slip with slightly faster net slip along the eastern half of the fault plane. Transfer of slip from the adjacent Coyote Hills fault to the east produces greater energy release rate on the eastern (overlapping) edge of the Santa Fe Springs fault than the western (leading) edge.

slip transfer zones has been observed in analog experiments (e.g. Mansfield and Cartwright, 2001) and modeled (e.g. Willemse and Pollard, 2000). Similarly, the eastern edge of the Santa Fe Springs fault has high-energy release rate demonstrating potential for linkage with the Coyote Hills fault to the east. Although slip vectors along the Santa Fe Springs fault are primarily dip-slip, larger net slip occurs along the eastern edge of the Santa Fe Springs than the western edge (Fig. 5) due to interaction with the adjacent Coyote Hills fault.

The change in energy release rate along the western tips of the faults in successive models gives evidence for the potential for westward propagation of the fault system (Fig. 3C and E). The drop in energy release rate on the western tip of the Coyote Hills fault, with the addition of the Santa Fe Springs fault reflects a drop in slip along the westernmost elements of the Coyote Hills fault due to interaction with the Santa Fe Springs fault. Thus, with both the Santa Fe Springs and the Coyote Hills faults accommodating strain as fault slip, the propagation potential of the western tip of the Coyote Hills fault decreases. Interestingly, although they are juxtaposed, the eastern tip of the Santa Fe Springs fault has a much greater propagation potential than the western tip of the Coyote Hills fault. Thus, the linkage of these faults, suggested by the high-energy release rate, may be dominated by the Santa Fe Springs fault.

The drop in energy release rate on the western tip of the Santa Fe Springs fault with the addition of the Los Angeles fault indicates another decrease in propagation potential. In contrast, on the eastern tip of the Santa Fe Springs fault propagation potential increases with the addition of the Los Angeles fault (Fig. 3F) suggesting once again that the Santa Fe Springs fault may extend farther east than currently modeled and link to the Coyote Hills fault (Fig. 3F).

6. Strain energy density

Strain energy density measures the elastic strain stored in the host rock around each fault (e.g. Jaeger and Cook, 1976). The strain energy density is the mechanical work performed by the rock surrounding the faults and is measured as (Jaeger and Cook, 1976):

$$V_0 = 1/2(\sigma_{xx}\varepsilon_{xx} + \sigma_{yy}\varepsilon_{yy} + \sigma_{zz}\varepsilon_{zz} + 2\sigma_{xy}\varepsilon_{xy} + 2\sigma_{xz}\varepsilon_{xz} + 2\sigma_{yz}\varepsilon_{yz}) \quad (4)$$

where V^0 represents strain energy per unit volume, σ_{ij} is the stress, ε_{ij} is the strain at a point within the system and the subscripts refer to the different normal and shear stresses and strains. The work term of internal strain energy density is found by integrating Eq. (4) throughout the model (Cooke and Murphy, 2004). For this study, we examine the distribution of strain energy density per unit volume throughout the entire modeled space. Although strain energy density only measures elastic strain, regions with greater than average elastic strain are likely to experience a larger amount of inelastic strain, such as microcracking, which could facilitate fault growth in the region. Thus, strain energy density can be used to estimate the locations of new failure and the propagation of faults (e.g. Du and Aydin, 1993).

6.1. Strain energy density patterns

Extremely high values of strain energy density can occur along the fault near the boundaries between individual fault elements. These are artifacts of the model and depend on the discretization of the fault. Although use of smaller fault elements can reduce this effect, some local effects are unavoidable. To interpret the strain energy density pattern, we avoid variations along the faults and focus on the largest regions of higher than average strain energy density. Regions larger than the size of the fault elements are not artifacts of discretization and reflect the focusing of strain due to the modeled faulting.

In model 1, the average strain energy density is about 2.5×10^{-3} MPa and the isosurface of this value outlines two regions of higher than average strain energy density (A and B on Fig. 6a). The first region, at the eastern tip of the modeled Whittier fault, is an artifact of the model because the modeled tip does not represent the true eastern tip of the Whittier fault, which extends beyond the region modeled. Along the western tip of the Whittier fault is another region of high strain energy density (B on Fig. 6a). A tubular shaped isosurface extends well out in front of the fault, outlining a large region that may experience microcracking (Fig. 6a). This 2.5×10^{-3} MPa strain energy density isosurface at 9 km depth outlines regions directly to the northwest of the Whittier fault tip (along the fault trend) as well as a region south of the westernmost tip of the Whittier fault. The incipient Coyote Hills fault segment lies within the greater than average strain energy density region south of the western Whittier fault tip.

With the addition of the Coyote Hills segment in the second model, the 2.5×10^{-3} MPa strain energy density isosurface changes significantly (Fig. 6b). The isosurface now encompasses a larger volume around the end of both the Whittier and Coyote Hills faults, suggesting the strain energy density has increased in this region. At the same time, the dark regions on Fig. 6 indicating regions of strain energy density shadow (reduced strain energy density) have expanded. We expect that with the addition of faults, a greater degree of stored strain is released as fault slip, thereby extending the strain energy density shadows (e.g. Cooke and Murphy, 2004). At 8 km depth the region of higher than average strain energy density at the western edge of the Coyote Hills segment and Whittier faults has two lobes, one along the trend of the Coyote Hills segment and another along the trend of the Whittier fault (Fig. 6b). In addition to the tube of high strain energy density at the western edge of Coyote hills segment, the 2.5×10^{-3} MPa

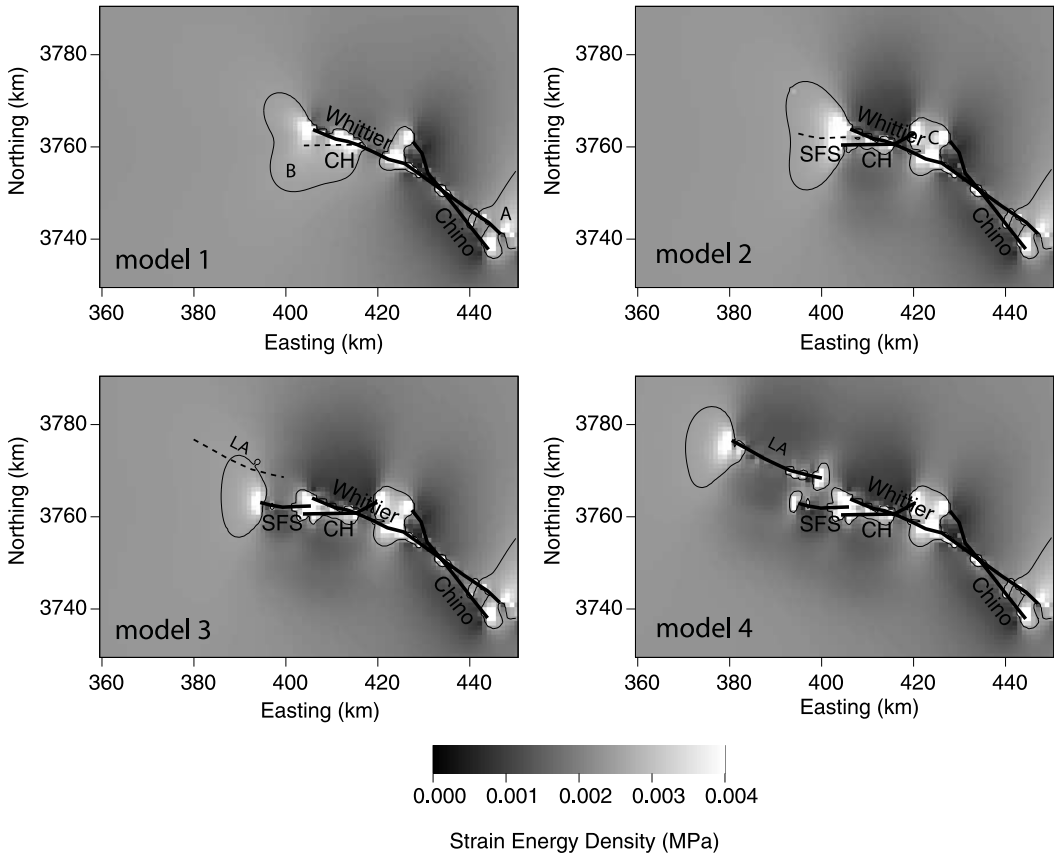

Fig. 6. Strain energy density at 8 km depth surrounding the successive models of the Puente Hills thrust system. The average strain energy density of the first model (0.0025 MPa) is contoured. Bright regions within the contoured line indicate high levels of elastic strain energy, representing regions with greater potential for failure. Existing faults in the model are shown in black, while incipient faults are shown dashed. CH, Coyote Hills segment, SFS, Santa Fe Springs segment and LA, Los Angeles segment of the Puente Hills thrust. Note the strong correlation between incipient fault location and regions of high strain energy density. Three-dimensional renderings of the strain energy distribution around the faults are available as interactive VRML files at http://www.geo.umass.edu/faculty/cooke/LA/LA.html.

strain energy density isosurface outlines a small region of relatively high strain energy density along the eastern edge of the Coyote Hills segment between the lower portion of this fault and the Chino fault (C on Fig. 6b).

The addition of the Santa Fe Springs segment of the Puente Hills thrust in the third model causes a shift in the location of the high strain energy density to the western tip of the Santa Fe Springs segment (Fig. 6c). At 8 km depth this volume of high strain energy density is located slightly to the north and west of the leading tip of Santa Fe Springs fault, rather than directly west and along the Santa Fe Springs fault trend. The region of higher than average strain energy density at the western tip of the Coyote Hills segment in the previous model is reduced with the addition of the Santa Fe Springs segment in this model, although the high strain energy density between the eastern tip of the Coyote Hills and the Chino faults persists.

With the addition of the Los Angeles segment in model 4, the region of highest strain energy density again moves westward, to the western tip of the Los Angeles fault and the strain energy density at the west end of the Santa Fe Springs fault diminishes in volume (Fig. 6d). The high strain energy density at the western tip of the Los Angeles segment of the Puente Hills thrust is not meaningful because other faults in the region that are not included in these models would influence stresses in this region. However, the persistence of high strain energy density between the eastern tip of the Coyote Hills and Chino faults is not a model artifact.

6.2. Strain energy density pattern analysis

The largest volumes of high strain energy density are generally located on the western tip of the faults, suggesting a large amount of inelastic deformation within these regions that subsequently facilitates westward propagation of the system. In each of the first three models, tubes of higher than average strain energy density at the western tip of the fault systems partially envelope the area where the next fault occurs. For isolated faults, strain energy density is concentrated around the fault tip and along the trend of the fault. The deviations from this pattern observed in these model results indicate significant interaction among nearby faults. Consequently, the correlation of regions of higher than average strain energy density with incipient fault

location is especially compelling because these locations are generally not along the trend of but échelon to existing faults. At 8 km depth this is apparent in model 1 (Fig. 6a) where the lobe of high strain energy density south of the western tip of the Whittier fault encompasses the incipient Coyote Hills segment and at the western edge of model 3, where the high strain energy density is slightly north to the trend of Santa Fe Springs Fault, correctly predicting the Los Angeles fault location (Fig. 6c). Another outcome of the correlation of high strain energy density and locations of incipient faulting is that regions of high strain energy density near the leading lateral fault tip become regions of strain energy density shadow upon addition of the next fault. This leads to an asymmetry between strain energy density at leading and overlapping tips of fault segments.

In contrast to the western tips of the Puente Hills thrust faults, the eastern (overlapping) edges of the faults show small volumes of high strain energy density. The asymmetry in the distribution of strain energy density around the western and eastern fault edges reflects interaction with nearby faults; if the faults were isolated the dip-slip would be symmetrically distributed producing equal strain at both lateral tips of the fault. For example, the asymmetry of strain energy density between the western and eastern tip of the Los Angeles fault (Fig. 6D) suggests that the Los Angeles and Santa Fe Springs faults are interacting. Interestingly, the overlapping tips of these faults have small volumes of high strain energy density localized at each fault tip that do not extend into the overlap region suggesting that much of the overlap region is relatively undeformed. From the evidence for fault interaction and lack of deformation in the overlap zone we infer that these faults are soft-linked; these échelon segments act as one throughgoing fault surface and do not extensively strain the rock within the overlap zone (e.g. Maerten and Pollard, 2002). In contrast, the small region between the Santa Fe Springs and the Coyote Hills faults has large values of strain energy density, as does the region between the Coyote Hills and Chino faults at 8 km depth (Fig. 6). Large volumes of high strain energy density values suggest local failure and potential fault propagation in these locations. Such propagation may result in hard-linkage between the Santa Fe Springs and Coyote Hills faults as well as the Coyote Hills and Chino faults. These results support the inference from energy release rate results that these faults may be hard-linked. Furthermore, the three-dimensional pattern of strain energy density suggests that the potential linkage of the Coyote Hills fault to the Chino fault is strongest below ~7 km depth (http://www.geo.umass.edu/faculty/cooke/LA/LA.html).

7. Navier–Coulomb stress

Navier–Coulomb stress measures a combination of shear stress and normal stress that relates to the failure of intact rock (e.g. Jaeger and Cook, 1976). Navier–Coulomb stress, S_{nc}, on any plane is calculated as

$$S_{nc} = |\tau| - \mu\sigma \quad (5)$$

where τ is the shear stress on the plane, μ is the coefficient of internal friction and σ is the normal compressive stress on the plane. Failure occurs when S_{nc} is greater than or equal to the inherent shear strength of the rock measured in laboratory experiments. Correspondingly, we can derive the orientation of the plane with the greatest potential for failure, or greatest Navier–Coulomb stress at any point (e.g. Crider and Pollard, 1998; Maerten and Pollard, 2002; Ferrill and Morris, 2003). In addition to calculating the orientation of the planes of greatest Navier–Coulomb stress to predict the orientation of potential shear failure the distribution of Navier–Coulomb stress can be mapped in order to predict the locations that are closest to failure.

7.1. Locations of greatest Navier–Coulomb stress

Similarly to the strain energy density (Fig. 6), at 8 km depth, high Navier–Coulomb stresses occur within regions around and in front of the leading (westernmost) fault tips (Fig. 7). As segments of the Puente Hills thrust system are added, Navier–Coulomb stress concentrations are localized at the westernmost lateral fault tip. The region between the eastern tip of the Coyote Hills fault and the western tip of the Chino fault contains high Navier–Coulomb stress (Fig. 7), in agreement with the suggestion from strain energy density pattern that the faults my grow further into this region.

Some differences arise between the strain energy density and Navier–Coulomb stress patterns. The Navier–Coulomb stress results from model 1 indicate high failure potential north of the Whittier fault (Fig. 7); this is different from the strain energy density pattern and does not correlate with the incipient Coyote Hills fault location. Furthermore, from model 2 to models 3 and 4, a region of high Navier–Coulomb stress develops parallel to and south of the Coyote Hills and Santa Fe Springs faults. This region does not correlate within any recognized faults (Fig. 7).

7.2. Orientation of planes of maximum Navier–Coulomb stress

In addition to outlining regions of potential faulting, the Navier–Coulomb criterion predicts the orientation of two conjugate planes of greatest Navier–Coulomb stress. These planes are equally favored in a homogeneous isotropic system, but heterogeneity gives preference to one orientation. By comparing the orientation of predicted failure planes to the actual fault surfaces that developed, we are able to assess the viability of Navier–Coulomb stress in the study of fault growth. The orientations of the planes of maximum Navier–Coulomb stress are calculated at points on the western tip of each of the faults near 8 km depth. The

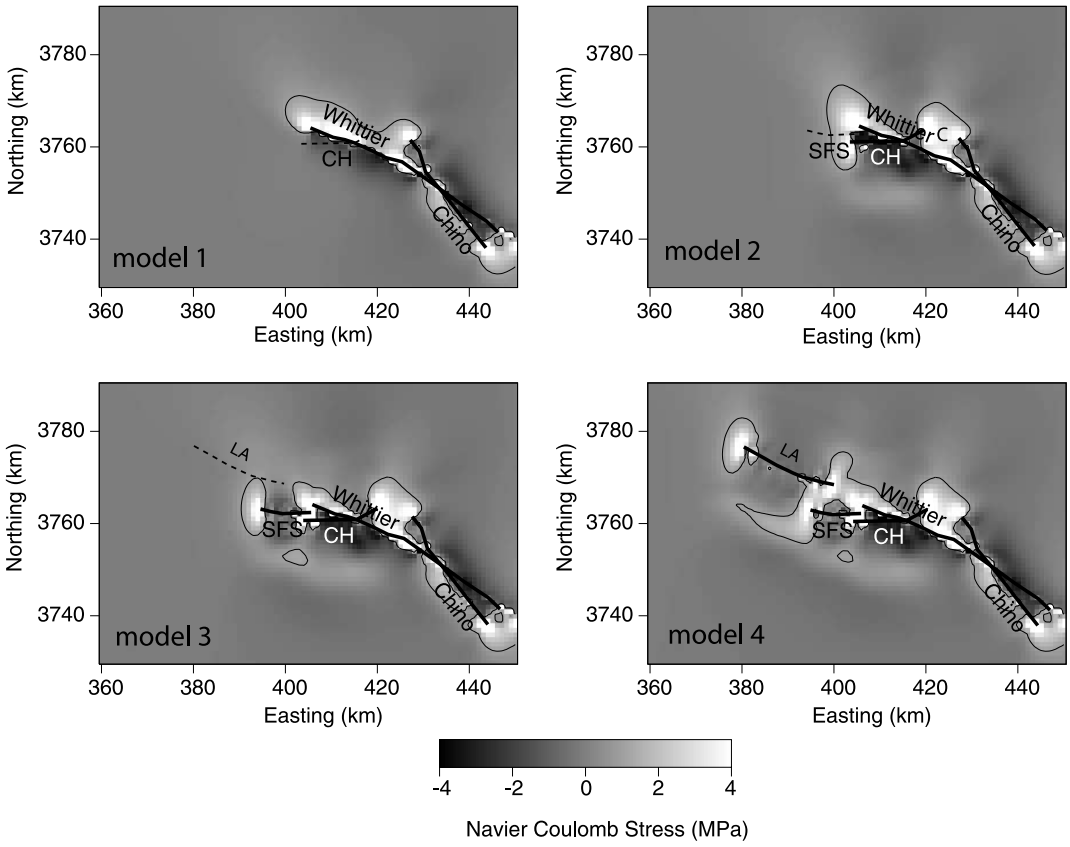

Fig. 7. Navier–Coulomb stress (MPa) at 8 km depth within the successive models of Puente Hills thrust fault development. Bright areas have greater failure potential than darker areas. The contour shows values of 1 MPa in order to highlight regions of Navier–Coulomb stress concentration. Incipient fault locations are dashed. CH, Coyote Hills segment, SFS, Santa Fe Springs segment and LA, Los Angeles segment of the Puente Hills thrust. The regions of high Navier–Coulomb stress do not correlate as well to locations of incipient faulting as do the regions of high strain energy density.

conjugate sets of planes are grouped such that set 1 contains the predicted failure planes closer to the true fault orientation.

Throughout the first three models, one of the conjugate planes of maximum Navier–Coulomb stress in each model accurately predicts the strike of the incipient fault (Fig. 8A and C). All of the strikes of set 1 are within 33° of the strikes of the incipient faults. The other conjugate plane is oriented almost perpendicular to the first plane and, consequently, lies perpendicular to the orientation of the incipient fault (Fig. 8B and C). However, the planes of set 1 consistently dip more steeply than the incipient fault; set 2 dips from 4° to as much as 30° more steeply than the observed faults (Fig. 8 A and C). No fault orientation predictions were made for model 4, which includes all Puente Hills thrust faults, because the Los Angeles segment represents the last fault in the Puente Hills thrust.

7.3. Navier–Coulomb stress analysis

We propose two hypotheses to explain the over-estimate of fault dip by the Navier–Coulomb stress. The Coyote Hills, Santa Fe Springs, and Whittier faults are only well constrained from seismic images to a depth of approximately 5 km. Therefore, the faults may be shallow in the region imaged, but steeper at depth. Such fault geometry may reflect a change in fault style where the

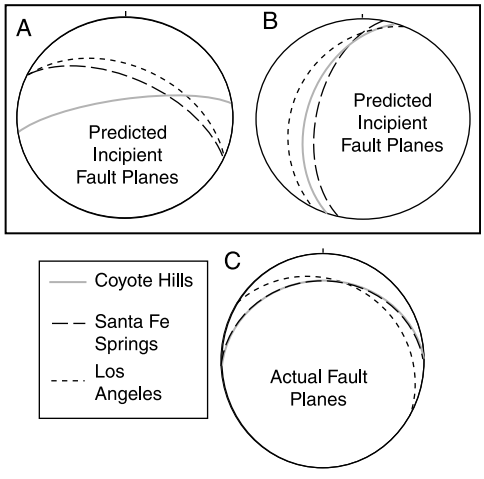

Fig. 8. Stereonets show the orientations of planes of maximum Navier–Coulomb stress (A and B) in the locations of incipient faulting, and the orientations of the faults of the Puente Hills thrust system (C). Note the similar orientation of the first set of predicted planes (A) and the actual fault orientations (C).

sediments that fill the Los Angeles basin to nearly 5 km depth facilitate bedding plane slip. Instead of the fault forming a continuous ramp through the sediments, the fault would have flat sections along the bedding planes and ramp sections across bedding to yield a more shallow dip than in the deeper bedrock. The Navier–Coulomb stress does not consider the effects of heterogeneous layers and predicts steeper than observed fault dips in the sedimentary strata. A steepening of the Santa Fe Springs fault below 5 km, while possible, conflicts with observed seismicity; the Whittier Narrows earthquake hypocenter has been interpreted to lie on the shallowly-dipping extension of the Santa Fe Springs at 17 km depth (Shaw and Shearer, 1999).

An alternative hypothesis, for the shallower than predicted dip of the faults, is based on the distribution of proto-faults. For example, if along the western tip of the Coyote Hills fault in the second model (the model prior to the addition of the Santa Fe Springs fault) an array of proto-faults form at the Navier–Coulomb stress predicted dip (59°) at every point along the western tip of the Coyote Hills fault, the overall pattern of proto-faults follows the Coyote Hills fault (dipping 30°). These fractures could then link up forming a fault plane dipping similarly to the Coyote Hills fault and more shallowly than the predicted planes of maximum Navier–Coulomb stress. Furthermore, this overall alignment of steep micro-fractures would be encompassed within the shallow-dipping high strain energy density tube west of the existing fault tip (Fig. 2).

8. Conclusions

Energy-release rate, strain-energy density and Navier–Coulomb stress all predict some aspect of incipient fault geometry (location and orientation). The energy release rate at the leading western tip of the fault system decreases with the addition of each new fault to the west; fault tips with high energy release rate correlate with the direction of incipient lateral growth of the fault system. Although the energy release rate can be used to assess the location of incipient faulting, this method presumes that the fault system grows via propagation from the tips of existing faults. For this échelon system modeled here, such presumptions fall short of predicting accurate fault growth.

Within models 1–3, each incipient fault is partially encompassed by a tube of high strain energy density at the leading (western) tip of the fault system. At a depth of 8 km, the locations of incipient faults are more strongly correlated to regions of higher than average strain energy density than regions of high Navier–Coulomb stress, suggesting that strain energy density pattern may be a more reliable predictor of incipient fault location. The correlation is particularly compelling for the prediction of the échelon nature of the fault system.

One of the two planes of maximum Navier–Coulomb stress ahead of the faults correlates well with incipient fault strike. However, this method of predicting fault orientation appears less reliable for predicting the dip of incipient faults, which may better correlate to the dip of the volumes of high strain energy density.

In addition to predicting incipient fault geometry, energy release rate and strain energy density may provide insight into fault linkage. Within these models, large energy release rate along lateral fault tips and presence of high strain energy density between échelon fault segments suggests hard linkage of the segments. In contrast, low energy release rate and limited volumes of high strain energy density indicate that soft-linked faults may transfer slip effectively.

Using each of these fault propagation factors in concert constrains the growth of the fault system more than any one factor can alone. Energy release rate, strain energy density and Navier–Coulomb stress can be combined with up-to-date data sets of displacement distribution and slip maxima to further unravel the fault growth. In studies that can only implement one of these three factors, strain energy density may prove the most useful. Within the échelon thrust system model here, strain energy density predicts both future fault location and dip, while energy release rate is limited to overall direction of growth and Navier–Coulomb stress is best at predicting incipient fault strike.

Acknowledgements

We thank John Shaw for his insight into the geometry and growth of the Puente Hills thrust system. We also thank Simon Kattenhorn, Ron Bruhn and David Ferrill for helpful reviews that improved the manuscript. The Commonwealth College of the University of Massachusetts Amherst supported this work, which formed Erik Olson's undergraduate thesis. Poly3d software was provided by David Pollard of Stanford University.

References

Argus, D.F., Heflin, M.D., Donnellan, A., Webb, F.H., Dong, D., Hurst, K.J., Jefferson, G.A., Lyzenga, M., Watkins, M., Zumberge, J.F., 1999. Shortening and thickening of metropolitan Los Angeles measured and inferred by using geodesy. Geology 27, 703–706.

Childs, C., Nicol, A., Walsh, J.J., Watterson, J., 2003. The growth and propagation of synsedimentary faults. Journal of Structural Geology 25, 633–648.

Cooke, M.L., Kameda, A., 2002. A two-dimensional analysis using mechanical efficiency. Journal of Geophysical Research 107.

Cooke, M.L., Murphy, S., 2004. Assessing the work budget and efficiency of fault systems using mechanical models. Journal of Geophysical Research 109.

Cox, S.J.D., Scholz, C.H., 1988. Rupture initiation in shear fracture of rocks: an experimental study. Journal of Geophysical Research 93, 3307–3320.

Crider, J.G., Pollard, D.D., 1998. Fault linkage: 3D mechanical interaction between échelon normal faults. Journal of Geophysical Research 103, 24373–24391.

Crouch, S.L., Starfield, A.M., 1990. Boundary Element Method in Solid Mechanics. Unwin Hyman, Boston, MA.

Dawers, N.H., Underhill, J.R., 2000. The role of fault interaction and linkage in controlling syn-rift stratigraphic sequences: Statfjord East area, Northern North Sea. AAPG Bulletin 84, 45–64.

Dolan, J.F., Sieh, K.E., Rockwell, T.K., Yeats, R.S., Shaw, J., Suppe, J., Huftile, G., Gath, E., 1995. Prospects for larger or more frequent earthquakes in the greater metropolitan Los Angeles. Science 267, 188–205.

Dolan, J.F., Christofferson, S.A., Shaw, J.H., 2003. Recognition of paleoearthquakes on the Puente Hills Blind Thrust Fault, California. Science 300, 115–118.

Du, Y., Aydin, A., 1993. The maximum distortional strain energy density criterion for shear fracture propagation with applications to the growth paths of en échelon faults. Geophysical Research Letters 20, 1091–1094.

Feigl, K.L., Agnew, D.C., Bock, Y., Dong, D., Donnellan, A., Hager, B.H., Herring, T.A., Jackson, D.D., Jordan, T.H., King, R.W., Larsen, S., Larson, K.M., Murray, M.H., Shen, Z., Webb, F.H., 1993. Space geodetic measurement of crustal deformation in Central and Southern California, 1984–1992. Journal of Geophysical Research 98, 21677–21712.

Ferrill, D.A., Morris, A.P., 2003. Dilational normal faults. Journal of Structural Geology 25, 183–196.

Griffith, W.A., Cooke, M.L., 2004. Mechanical validation of the three-dimensional intersection geometry between the Puente Hills blind-thrust system and the Whittier fault, Los Angeles, California. Bulletin of the Seismological Society of America 94, 493–505.

Griffith, W.A., Cooke, M.L. How sensitive are fault slip rates in the Los Angeles to tectonic boundary conditions? Bulletin of the Seismological Society of America 95, 1263–1275.

Gupta, S., Cowie, P.A., Dawers, N.H., Underhill, J.R., 1998. A mechanism to explain rift-basin subsidence and stratigraphic patterns through fault-array evolution. Geology 26, 595–598.

Ingersoll, R.V., Rumelhart, P.E., 1999. Three-stage evolution of the Los Angeles Basin, Southern California. Geology 27, 593–596.

Jaeger, J.C., Cook, N.G.W., 1976. Fundamentals of Rock Mechanics. Chapman and Hall, London. 585pp.

Kattenhorn, S., Pollard, D., 1999. Is lithostatic loading important for the slip behavior and evolution of normal faults in the Earth's crust? Journal of Geophysical Research 104, 28879–28898.

Kattenhorn, S.A., Pollard, D.D., 2001. Integrating 3-D seismic data, field analogs, and mechanical models in the analysis of segmented normal faults in the Wytch Farm oil field, southern England, United Kingdom. AAPG Bulletin 85, 1183–1210.

Lawn, B., 1993. Fracture of Brittle Solids, Cambridge University Press, New York, second ed. 378pp.

Li, V.C., 1987. The mechanics of shear rupture applied to earthquake zones. In: Atkinson, B.K. (Ed.), Fracture Mechanics of Rock. Academic Press. 534pp.

Maerten, L., Pollard, D., 2002. Effects of local stress perturbation on secondary fault development. Journal of Structural Geology 24, 145–153.

Mansfield, C., Cartwright, J., 2001. Fault growth by linkage: observations and implications from analogue models. Journal of Structural Geology 23, 745–763.

Marchal, D., Guiraud, M., Rives, T., van den Driessche, J., 1998. Space and time propagation processes of normal faults. In: Jones, G., Fisher, Q.J., Knipe, R.J. (Eds.), Faulting, Sealing and Fluid Flow in Hydrocarbon Reservoirs. Geological Society Special Publication, vol. 147, pp. 51–70.

Meigs, A., Cooke, M., 2004. Ground truth: boundary element models of northern LA basin CFM faults versus patterns of folding and rock uplift since 2.9 M., Southern California. Earthquake Center Annual Meeting.

Meyer, V., Nicol, A., Childs, C., Walsh, J.J., Watterson, J., 2002. Progressive localisation of strain during the evolution of a normal fault population. Journal of Structural Geology 24, 1215–1231.

Pivnik, D.A., Ramzy, M., Steer, B.L., Thorseth, J., El Sisi, Z., Gaafar, I., Garing, J.D., Tucker, R.S, 2003. Episodic growth of normal faults as recorded by syntectonic sediments, July oil field, Suez Rift, Egypt. AAPG Bulletin 87, 1015–1030.

Pollard, D.D., Aydin, A., 1988. Progress in understanding jointing. Geological Society of America Bulletin 100, 1181–1204.

Schneider, C., Hummon, C., Yeats, R., Huftile, G., 1996. Structural evolution of the northern Los Angeles basin, California, based on growth strata. Tectonics 15, 341–355.

Scholz, C.H., 2002. Mechanics of Earthquakes and Faulting 2002. 471pp.

Shaw, J.H., Shearer, P.M., 1999. An elusive blind thrust beneath metropolitan Los Angeles. Science 283, 1516–1518.

Shaw, J.H., Suppe, J., 1996. Earthquake hazards of active blind-thrust faults under the central Los Angeles basin, California. Journal of Geophysical Research 101, 8623–8642.

Shaw, J.H., Plesch, A., Dolan, J., Pratt, T., Fiore, P., 2002. Puente Hills blind-thrust system, Los Angeles, California. Bulletin of the Seismological Society of America 92, 2946–2960.

Spyropoulos, C., Scholz, C., Shaw, B., 2002. Transition regimes for growing crack populations. Physical Review 65, 056105.

Thomas, A.L., 1993. Poly3D: A Three-Dimensional, Polygonal Element, Displacement Discontinuity Boundary Element Computer Program with Applications to Fractures, Faults, and Cavities in the Earth's Crust. MS Thesis, Geology Department, Stanford University, 52pp.

Thomas, A.L., Pollard, D.D., 1993. The geometry of échelon fractures in rock: implications from laboratory and numerical experiments. Journal of Structural Geology 15, 323–334.

Walsh, J.J., Bailey, W.R., Childs, C., Nicol, A., Bonson, C.G., 2003. Formation of segmented normal faults: a 3-D perspective. Journal of Structural Geology 25, 1251–1262.

Willemse, E.J.M., Pollard, D.D., 2000. Normal fault growth; evolution of tipline shapes and slip distribution. In: Lehner, F.K., Urai, J.L. (Eds.), Aspects of Tectonic Faulting. Springer, Berlin, pp. 193–226.

Wong, T.F., 1982. Shear fracture energy of Westerly granite from post failure energy. Journal of Geophysical Research 87, 990–1000.

Wright, T.L., 1991. Structural geology and evolution of the Los Angeles basin, California. In: Biddle, K.T. (Ed.), Active Margin Basins. American Association of Petroleum Geologists Memoir, Tulsa, OK, pp. 35–134.

Young, M.J., Gawthorpe, R.L., Hardy, S., 2001. Growth and linkage of a segmented normal fault zone; the Late Jurassic Murchison–Statfjord North Fault, northern North Sea. Journal of Structural Geology 23, 1933–1952.